

Full length article

Dendritic evolution during coarsening of Mg-Zn alloys via 4D synchrotron tomography



Enyu Guo ^{a, b, **}, A.B. Phillion ^{b, c}, Biao Cai ^{a, b}, Sansan Shuai ^{b, d}, Daniil Kazantsev ^{a, b}, Tao Jing ^d, Peter D. Lee ^{a, b, *}

^a School of Materials, University of Manchester, Manchester, M13 9PL, UK

^b Research Complex at Harwell, RAL, Didcot, OX11 0FA, UK

^c Department of Materials Science and Engineering, McMaster University, Hamilton, L8S 4L7, Canada

^d School of Materials Science and Engineering, Tsinghua University, Beijing, 100084, China

ARTICLE INFO

Article history:

Received 26 July 2016

Received in revised form

5 October 2016

Accepted 9 October 2016

Available online 31 October 2016

Keywords:

Magnesium alloy

Semi-solid

X-ray tomography

Coarsening

Dendrite

ABSTRACT

The scale of solidification microstructures directly impacts micro-segregation, grain size, and other factors which control strength. Using *in situ* high speed synchrotron X-ray tomography we have directly quantified the evolution of dendritic microstructure length scales during the coarsening of Mg-Zn hcp alloys in three spatial dimensions plus time (4D). The influence of two key parameters, solute composition and cooling rate, was investigated. Key responses, including specific surface area, dendrite mean and Gauss curvatures, were quantified as a function of time and compared to existing analytic models. The 3D observations suggest that the coarsening of these hcp dendrites is dominated by both the remelting of small branches and the coalescence of the neighbouring branches. The results show that solute concentration has a great impact on the resulting microstructural morphologies, leading to both dendritic and seaweed-type grains. It was found that the specific solid/liquid surface and its evolution can be reasonably scaled to time with a relationship of $\sim t^{-1/3}$. This term is path independent for the Mg-25 wt%Zn; that is, the initial cooling rate during solidification does not greatly influence the coarsening rate. However, path independence was not observed for the Mg-38 wt%Zn samples because of the seaweed microstructure. This led to large differences in the specific surface area (S_s) and its evolution both between the two alloy compositions and within the Mg-38 wt%Zn for the different cooling rates. These findings allow for microstructure models to be informed and validated to improve predictions of solidification microstructural length scales and hence strength.

© 2016 Acta Materialia Inc. Published by Elsevier Ltd. This is an open access article under the CC BY license (<http://creativecommons.org/licenses/by/4.0/>).

1. Introduction

The process of solidification usually results in the formation of dendritic, tree-like patterns at the scale of the microstructure. Dendrites consist of complex primary, secondary, tertiary and sometimes higher-order branches. The growth of dendrites from the liquid melt is usually accompanied by coarsening, a change in shape driven by variations in interfacial curvature, decreasing the total interfacial area and hence free energy, resulting in a

concomitant increase in secondary dendrite arm spacing [1]. This coarsening process is most visible in the regions between the tips and the roots of the dendrites [1,2].

Understanding dendrite coarsening is of particular technological importance. The mechanical properties of industrial alloys are directly determined by the underlying microstructure. For example, the tensile strength of Al-Si alloys increases with a decrease in the secondary dendrite arm spacing [3,4], due to the resulting reduction in interdendritic structures and defects such as porosity and hot-tearing [5,6]. Coarsening also affects processing, for example, thixoforming requires a semi-solid structure with relatively fine and round grains [7], which can behave very differently to dendritic ones [8,9].

The thermodynamic driving force for dendritic coarsening is the need to decrease the total free energy of the system. This is achieved by reducing the dendrite interfacial curvature [10,11] and

* Corresponding author. School of Materials, University of Manchester, Manchester, M13 9PL, UK.

** Corresponding author. School of Materials, University of Manchester, Manchester, M13 9PL, UK.

E-mail addresses: enyu.guo@manchester.ac.uk (E. Guo), peter.lee@manchester.ac.uk (P.D. Lee).

hence decreasing the total interfacial area. Thus, the process of dendritic coarsening occurs in a very similar way to Ostwald ripening [12], in which small particles having high interfacial curvature dissolve and redeposit onto larger ones with low interfacial curvature [12,13] due to the Gibbs-Thomson effect. Initial research on dendritic coarsening [14–16] found that the most useful quantifiable parameter was the secondary dendrite arm spacing λ_2 , and that this spacing varied as: $\lambda_2 \sim t_s^{1/3}$, where t_s is the local solidification time. Further research [7] has shown that λ_2 is insufficient to describe coarsening of microstructures with complex morphologies, nor does it describe coarsening once the microstructure has evolved to a more rounded geometry at longer times. Marsh and Glicksman [10] instead suggested using the specific interfacial area, S_v , as the characteristic length. Studies have shown that this parameter evolves as [10,11],

$$S_v^{-3}(t) - S_v^{-3}(0) = K_c t \quad (1)$$

where t is the coarsening time, $S_v(0)$ is the specific surface area at $t = 0$, and K_c the coarsening rate. Recently, the use of the solid-liquid interfacial curvature has been introduced to correlate microstructure to the dendritic coarsening process [17,18]. The evolution of dendritic coarsening is always associated with a change in local morphology, thus the quantification of the dynamic evolution of curvatures is of key importance when characterising coarsening processes.

Due to the importance of coarsening, a number of theoretical studies [19–22], including phase-field modeling [23,24], and experimental investigations [2,18,25–35] have been undertaken to study coarsening phenomena during solidification or under isothermal conditions in metallic alloy systems. Experimental studies of coarsening in metallic alloys are limited due to the difficulties involved in observing changes in microstructure directly as they occur. Prior *ex situ* studies of dendritic coarsening have mainly been performed on Al-Cu alloys [2,18,25,26,35], and Pb-Sn alloys [25,27] that were quenched after an isothermal hold of known duration. In those studies, the assumption was made that the cooling rate during quenching was sufficiently high enough to ‘freeze’ the semi-solid dendritic structure. 2D metallography [2,28,29] and 3D serial sectioning techniques [17,25,30] were then used to characterize the obtained microstructure. Although these studies provided insight into the mechanisms of coarsening, the 2D metallography results do not reflect the full 3D microstructure, and 3D serial sectioning is extremely time-consuming. Further, for both 2D and 3D *ex situ* studies, the observations are often difficult to interpret since each experiment is a single snapshot of an independent quenched microstructure (which may have evolved during quenching [31]), and hence they can only be statistically correlated.

The formation of dendrites and their subsequent coarsening is now the subject of many computational studies using a wide range of techniques from coupled control volume and front tracking techniques [36,37] to phase field [38,39] to combined analytic and numerical models. Many even include the influence of fluid flow [40]. However, there is a paucity of quantitative experimental data in magnesium alloys to both inform and validate these models [41].

With the advent of 3rd generation synchrotron sources, *in situ* 2D and 3D (or 4D, 3D plus time) imaging of microstructure development in metallic alloys is now possible. However, most of the experiments with semi-solid metals have focused on fcc aluminium alloys [42–45]. The resulting tomography datasets enable the temporal evolution of microstructure to be quantified in 3D and physical mechanisms to be explored. In a few instances, this methodology has been applied to dendritic coarsening in Al alloys. Limondin et al. [1] observed the dendritic evolution of an Al-10 wt% Cu alloy during solidification via *in situ* tomography, and found that

at low cooling rates, both growth and coarsening mechanisms played active roles in creating a very coarse dendritic structure. Terzi et al. [32] examined the coarsening process in the same alloy system, and observed the coexistence of three coarsening mechanisms on secondary dendrites: (i) melting of small dendritic arms, (ii) gradual movement of the dendrite root towards the dendrite tip, and (iii) dendrite coalescence and groove advancement. Fife et al. [46] studied the dynamic morphological evolution of the solid-liquid interface in semi-solid Al-Cu alloys at different volume fractions of solid, and quantified the relationship between interface curvature and velocity.

These synchrotron 4D imaging studies on dendritic coarsening have focused on Al-Cu alloys with fcc crystal structure because the semi-solid is relatively inert due to the stable oxide, and there is a substantial difference in contrast between the two phases. Currently, there is still a paucity of experimental data qualifying the coarsening process in alloys with hcp structure, including magnesium alloys. Such studies are required to both inform and validate microstructural models in this important class of alloys [41].

In the present research, dendritic coarsening in reactive Mg alloys with hcp crystal structure is studied *in situ* via high speed synchrotron tomography using a novel encapsulation system [47]. Specifically, the effects of alloy composition and cooling rate are examined. From the resulting datasets, the 3D dendritic microstructural evolution was quantified in terms of specific surface area (S_s) and interfacial curvature to reveal new insight into coarsening mechanisms in hcp metals and to provide quantitative time-evolved data for validation of microstructure models.

2. Materials and experimental methods

Mg-25 wt%Zn and Mg-38 wt%Zn alloys were selected to study. The use of a high Zn content enhances the X-ray absorption contrast between the liquid and solid phases, enabling the dendritic structures to be captured. The solidification range of the two alloys is $\sim 209^\circ\text{C}$ ($550\text{--}341^\circ\text{C}$) and $\sim 139^\circ\text{C}$ ($480\text{--}341^\circ\text{C}$), respectively. The alloys were prepared by mixing pure Mg and Zn powders in a stainless steel crucible under a protective atmosphere of CO_2 and SF_6 . The mixtures were then melted and cast into a graphite mould. Small cylindrical samples of ~ 1.5 mm in diameter were then machined from the casting for the coarsening experiments. The samples were then individually enclosed in a quartz encapsulation system [47] to eliminate oxidation effects and safety risks involved when melting Mg alloys.

The *in situ* tomography studies were performed at the Diamond-Manchester Beamline (I13) of the Diamond Light Source. A bespoke PID controlled furnace was used [43]. The coarsening experiments were carried out as follows. First, each sample was heated slowly to $\sim 30^\circ\text{C}$ above the liquidus temperature and then held for 20 min to ensure complete melting. Second, each sample was cooled at a rate of $25^\circ\text{C}/\text{min}$ to a temperature within the semi-solid region (490°C for Mg-25 wt%Zn and 410°C for Mg-38 wt%Zn), and then held for 60–90 min (depending on the sample) to allow coarsening to occur. Third, the process was repeated but at a slower cooling rate of $3^\circ\text{C}/\text{min}$ prior to the isothermal hold. Thus, for each alloy composition, the coarsening kinetics of the microstructure resulting from two different cooling rates (25 and $3^\circ\text{C}/\text{min}$) were studied.

Note that for isothermal semi-solid coarsening processes, and solidification studies in general, accurate knowledge of the temperature variation with time is critical. However, direct measurement of the sample's temperature was not possible during these experiments because of encapsulation. Instead, the temperature was measured in the furnace adjacent to the sample and the offset calibrated by quantifying the volume fraction of solid visible in the tomographic image at the beginning of the isothermal hold stage of

each test and adjustment using the equilibrium phase diagram. The offset was assumed constant during each experiment. For the two alloys (Mg-25 wt%Zn and Mg-38 wt%Zn), the measured fraction solid at the start of isothermal holding was 0.38 and 0.23, respectively, corresponding to the temperature of ~490 °C and ~410 °C, for Mg-25 wt%Zn and Mg-38 wt%Zn.

Concurrent with the coarsening experiments, X-ray tomography images were acquired using a pink beam (energy range 15–30 keV) and a PCO Edge 5.5 CMOS camera that was optically coupled to a single crystal CdWO₄ scintillator. The camera was binned to 1280 × 1080 pixels, resulting in a pixel size of 1.6 μm. For each tomography scan, a total of 1200 projections were collected over a 180° rotation with an exposure time of 10 ms and an additional 2 ms for the camera to readout the projection images. At the end of each tomographic scan, the sample stage was rotated back to –90° followed by pause for system re-initialization. The resulting total scan-to-scan cycle time was ~53 s of which only 14.4 s was used to actually acquire the tomographic data. Thus, in total, approximately 300 tomographic images were captured (75 for each cooling rate/ alloy combination).

After acquiring the projections, the tomographs were reconstructed using a filtered-back projection algorithm. Each dataset was then cropped and analysed using the ImageJ (NHS, US) and Avizo® (FEI, France) software tools. 3D anisotropic diffusion and median filters were applied to the cropped dataset to reduce the noise. The dendritic features were then segmented using a global threshold value, and the volume, surface area and surface curvatures were quantified.

3. Results and discussion

3.1. Qualitative observations of solidification and isothermal coarsening in Mg

3.1.1. General microstructural evolution

In this study of isothermal semi-solid coarsening processes, the following parameters were investigated: cooling rate to the isothermal hold temperature (and hence initial structure), hold time, and alloy composition. Fig. 1 provides an overview of the experimental results. This figure shows longitudinal slices extracted from the tomographic images, taken both before and after the isothermal coarsening, along with a 3D view of individual grains. Images are shown for each alloy and condition: Mg-25 wt%Zn and Mg-38 wt%Zn, cooled at both 25°C/min and 3°C/min prior to coarsening. A number of salient features can be observed. Looking first at the initial semi-solid microstructures, Fig. 1 (a-1, b-1, c-1, d-1), the dendrites in Mg-25 wt%Zn were smaller than in Mg-38 wt% Zn for the same cooling rate; this demonstrates that increasing the Zn content alters the solute growth restriction and hence tip radius of dendrites. Similarly, the faster cooling rate of 25°C/min resulted in finer microstructures as compared to 3°C/min.

Analysis of the tomography datasets acquired during the solidification stage showed that the Mg-Zn dendrites nucleated heterogeneously, on the oxide skin of the sample and the pre-existing porosity within the melt. After nucleation, the dendrites that nucleated on both the wall grew towards the centre of the sample and those that nucleated within the central region tended to grow in all directions, forming very complicated branching structures.

Concerning coarsening, a comparison of the images prior-to, and post, isothermal hold clearly shows that the morphology of the small grains initially cooled at 25°C/min has changed significantly (Fig. 1 (a-1, a-2) and (c-1, c-2)), evolving from a dendritic microstructure to a globular shape. In contrast, only slight morphological changes are evident after the isothermal hold for ~60 min is applied to large grains initially cooled at 3°C/min (Fig. 1

(b-1, b-2) and (d-1, d-2)). Coarsening during the isothermal hold is a diffusion-controlled process [12] driven by curvature, therefore the slowly cooled structures coarsen more slowly than the quickly cooled ones which are much finer and have high curvatures.

3.1.2. 3D dendrite morphology evolution

Time-resolved images of the coarsening process for individual dendrites are shown in Figs. 2–5 for both alloy compositions and cooling rates. By comparing these images, new insight can be elucidated.

First, a variation in Zn content strongly affects the microstructure of Mg alloys. In the case of Mg-25 wt%Zn, six-fold symmetry in the basal plane is clearly visible (Figs. 2(a) and 3(d)). With an increase in Zn composition to 38 wt%, the dendritic morphology of individual grains becomes highly branched, forming a seaweed-like structure. The seaweed structure, with many split tips, is easily discerned for the slow cooling rate case (Fig. 5) but less so in the higher cooling rate (Fig. 4). It is likely that the anisotropy introduced by the addition of high Zn content modifies the interfacial energy, altering both the dendritic growth directions and the morphology to different effects depending on cooling rate [48–52]. Yang et al. [48] recently performed a systematic X-ray tomography study of quenched Mg-Zn alloys, showing that the dendritic structure in rapidly cooled specimens breaks down for Zn content between 25 wt% and 40 wt% Zn, forming instead an apparent seaweed structure as the dendrite morphology changes from 18-branch at 20 wt%Zn to 12-branch at 45 wt%Zn. The pattern of dendritic structure observed in the present study largely matches these earlier findings, that is, at 25 wt%Zn a six-fold symmetry in the basal plane is observed, with each grain containing 18 or more branches. However, for compositions in the 35–40 wt%Zn range a strong seaweed structure was observed. Note that the differences in cooling conditions should be carefully considered when comparing the results from different studies. In Yang et al.'s study the sample was directly quenched from the liquid metal; in this study, the slower cooling rate during solidification enabled tip-splitting even at lower Zn levels of 25 wt%. This cooling rate dependence was not reported in Yang et al.'s study.

Second, the change in morphology during coarsening for initially high curvature (small) dendrites, Figs. 2 and 4 (also see supplementary video 1 and 2), is more significant than those that are large, Figs. 3 and 5 (also see Fig. 1 for direct comparison). In the case of dendrites in Mg-25 wt%Zn cooling at 25°C/min, it is interesting to observe that the coarsening process occurred 'group by group'; that is, the side branches in an array seen from the top view tended to evolve to six single large branches, as indicated by the numerals 1 to 6 in Fig. 2(f). The branches growing in the out-of-basal-plane direction were observed to evolve to a dimpled circular shape, i.e. with a deep hole. We hypothesize that this is due to the easier redistribution of solute between these close branches, leading to coarsening to occur faster than those spaced far apart. It would be interesting to see if microstructural models can predict this. In comparison, the change of dendritic morphology is not obvious for the same alloy, initially cooled at a slower rate of 3°C/min (Fig. 3). At this lower cooling rate, the dendrites grew to a larger size during the solidification portion of the experiment, concurrently coarsening during growth. A similar comparison can also be found in the results of Mg-38 wt%Zn (see Figs. 4 and 5).

Supplementary video related to this article can be found at <http://dx.doi.org/10.1016/j.actamat.2016.10.022>.

Third, coarsening was observed to occur through two main mechanisms: coalescence of neighbouring branches (*Mechanism 1*); or via the dissolution of small branches to the benefit of large ones (*Mechanism 2*). *Mechanism 1* is highlighted in Fig. 3(g–i). Here it can be seen that two separate branches slowly merged into a

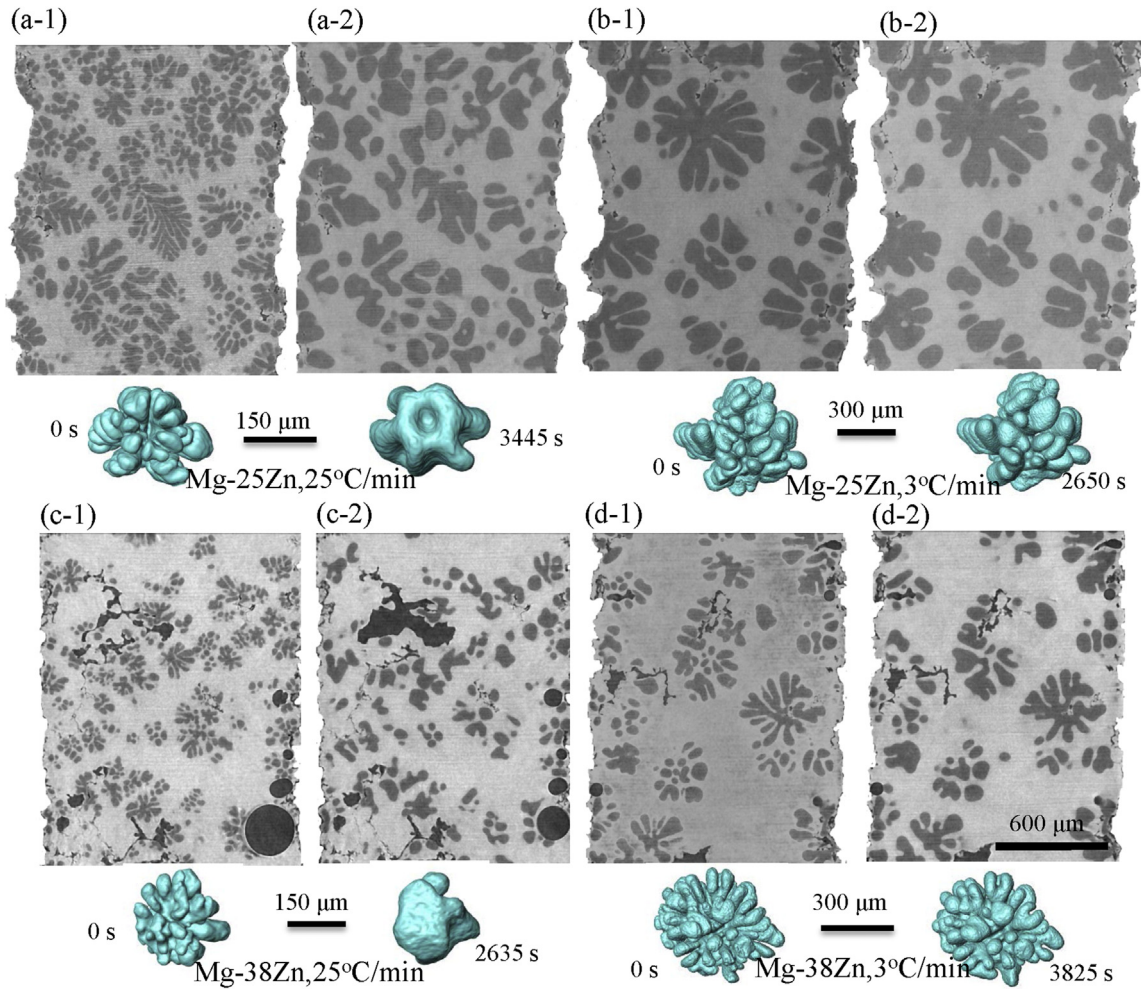


Fig. 1. Images showing the evolution of dendritic structures of Mg-25 wt%Zn (a-1, a-2, b-1, b-2) and Mg-38 wt%Zn (c-1, c-2, d-1, d-2) alloys before (time = 0 s) (a-1, b-1, c-1, d-1) and after (a-2, b-2, c-2, d-2) the isothermal hold stage for coarsening. Initial cooling rates were 3 °C/min for b-1 and d-1, and 25 °C/min for a-1 and c-1. 3D rendering of an individual dendrite before and after isothermal coarsening is also shown beneath each 2D slice. All the 2D slices share the same scale bar as d-2.

larger one through filling of the groove between them. This mechanism was frequently observed in all the experiments, as the process is independent of the difference in tip radii between neighbouring arms [53]. The high occurrence of tip-splitting in the Mg-38 wt%Zn experiments created a large number of grooves (as indicated by red arrows in Fig. 5(b) and (c)) which also favours the occurrence of Mechanism 1.

Mechanism 2, highlighted in Fig. 5(d–f), was also frequently observed. As can be seen, the small central branch dissolved gradually along its axis, rather than along the radii, and the surrounding dendrites increased in size. It is interesting to note that coarsening mechanisms frequently observed in Al-Cu alloy systems, including the coalescence of the branches by merging of the tips first, (e.g. Ref. [54]), radii melting [55], and fragmentation of the dendrite root [55], were not observed in these experiments. This is most likely attributed to the fact that the significant difference in dendritic morphologies in a hcp system as compared to a fcc system resulted in different solute redistribution within the arm space.

3.2. Quantitative analysis

3.2.1. Error estimation

Fig. 6 shows the evolution in dendrite volume for seven individual dendrites from Mg-25 wt%Zn (Fig. 6(a)) and Mg-38 wt%Zn

(Fig. 6(b)). This data provides an estimate of the thermal stability of the furnace, along with the accuracy of the process used to segment individual dendrites. For each curve, the volumes have been normalized by the maximum volume obtained from each dendrite over the entire experimental duration. The dendrites labelled as D2, D3, D5 and D7 in the figure correspond to those as shown in Figs. 2–5. As can be seen, the dendrite volume first increased during solidification, and then stabilized during the isothermal hold. A small fluctuation in volume, on the order of 1–4%, is present for each dendrite during the isothermal holding stage. There was no difference between the six-fold dendrites (Mg-25 wt%Zn, Fig. 6(a)) and the seaweed structure (Mg-38 wt%Zn, Fig. 6(b)). The fact that the normalized volume only changes very slightly is a good indication that errors due to thermal fluctuations and dendrite segmentation are small, allowing for quantitative analysis of the coarsening process based on the acquired 4D images.

3.2.2. Evolution in specific surface area

As discussed in the introduction, the evolution in specific surface area, S_v , has been widely adopted to quantify the overall evolution in microstructure during dendritic coarsening [2,10,11,21]. This can also be evaluated on each dendrite, where S_v becomes S_s (defined as solid-liquid interface area per unit volume enclosed by the interface). Fig. 7(a) shows the evolution of S_s for individual

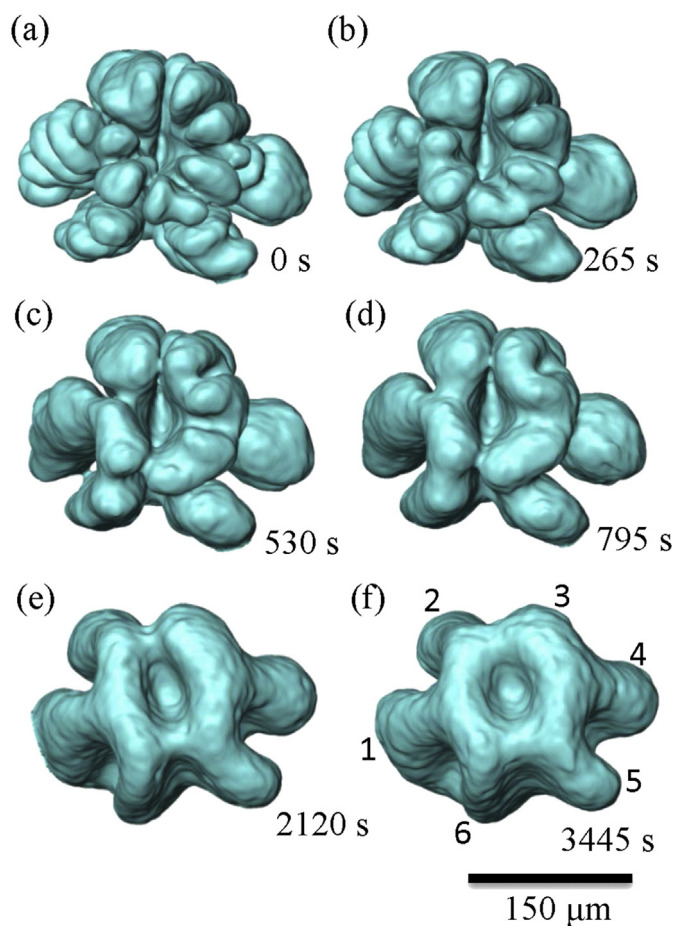


Fig. 2. Dendritic evolution of α -Mg in Mg-25 wt%Zn alloy during isothermal coarsening at -490 °C. Initial solidification cooling rate was 25 °C/min.

dendrites. It can be seen from the curves that S_s decreased quickly during solidification and then continuously decreased but with a much slower speed during the isothermal hold. The significant decrease of S_s during the solidification stage is due to the growing dendrites both increasing in volume and their contaminant coarsening, which when combined significantly outweighs the addition surface area created at the tips. During the isothermal hold, only coarsening is occurring, leading to a continuous decrease in S_s .

It has been shown in the studies by Voorhees et al. [18,46,56] that the inverse of specific surface area follows a $\sim t^{1/3}$ power law during isothermal dendritic coarsening. Fig. 7(b) shows plots of S_s^{-3} as a function of time, along with the linear fit curves. The corresponding isothermal coarsening rate constant, K_c ($\mu\text{m}^3/\text{s}$), of each dendrite can be evaluated directly from the slope of the fitted curves; these values are listed in Table 1. As can be seen, there is a significantly higher coarsening rate for the Mg-25 wt%Zn alloy as compared to the Mg-38 wt%Zn alloy. Thus, the coarsening process is closely related to the grain morphology induced by alloy concentration, i.e. the six-fold dendritic symmetry and the seaweed structures lead to different coarsening rates, or rather different initial states that alter the subsequent coarsening during isothermal hold. The lower isothermal hold temperature used to coarsen Mg-38 wt%Zn may also have retarded the coarsening process, as coarsening is a diffusion-controlled mechanism. However, the diffusion coefficient of Zn in liquid Mg at 410 °C is only 10% smaller as compared to the value at 490 °C, assuming that Einstein's relation [57] for estimating the diffusion coefficient of a Brownian

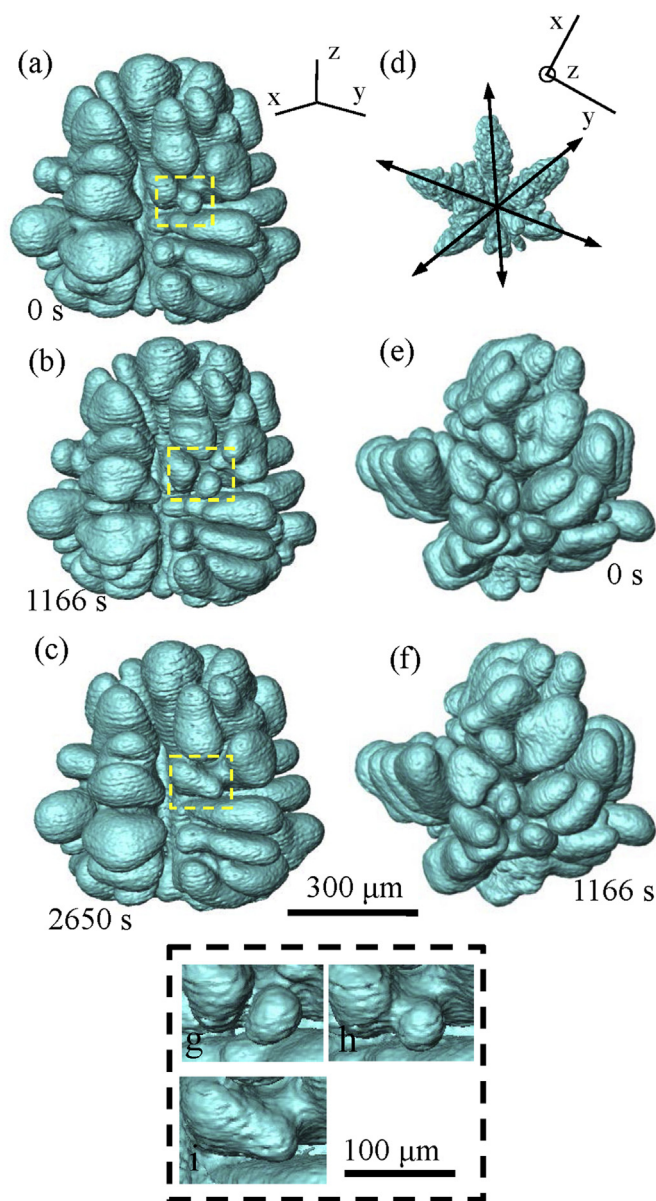


Fig. 3. Dendritic evolution of α -Mg in Mg-25 wt%Zn alloy during isothermal coarsening at -490 °C. Initial solidification cooling rate was 3 °C/min. Images of (a)–(c) are shown from lateral view, while (d)–(f) are from top view. The enlarged regions, as indicated by rectangle in (a)–(c), are shown in (g), (h), (i), respectively; the formation of six-fold structure of α -Mg dendrite in the basal plane is shown in (d) when the dendrite was first observed during cooling.

particle moving in a fluid holds true.

By comparing the dendrites analysed from Mg-25 wt%Zn (D1–D3), it can be seen that their coarsening rate constants (slopes of the fitted lines) are similar in value, indicating that the coarsening process is independent of the cooling path during solidification rather than, as shown in Figs. 2 and 3, linked to the size of the grain. This finding reinforces prior observations that dendritic evolution during isothermal coarsening follows a self-similarity rule [26,58–60]. In contrast, the situation for Mg-38 wt%Zn (D4–D7) is more complex. As shown in Table 1, the coarsening rate constant for the sample cooled at 25 °C/min is nearly twice that of the sample cooled at 3 °C/min. By comparing Fig. 4(a) and 5(a), it also appears that the initial structures are very different; at a cooling rate of 3 °C/min (Fig. 5(a)), the seaweed structure contains

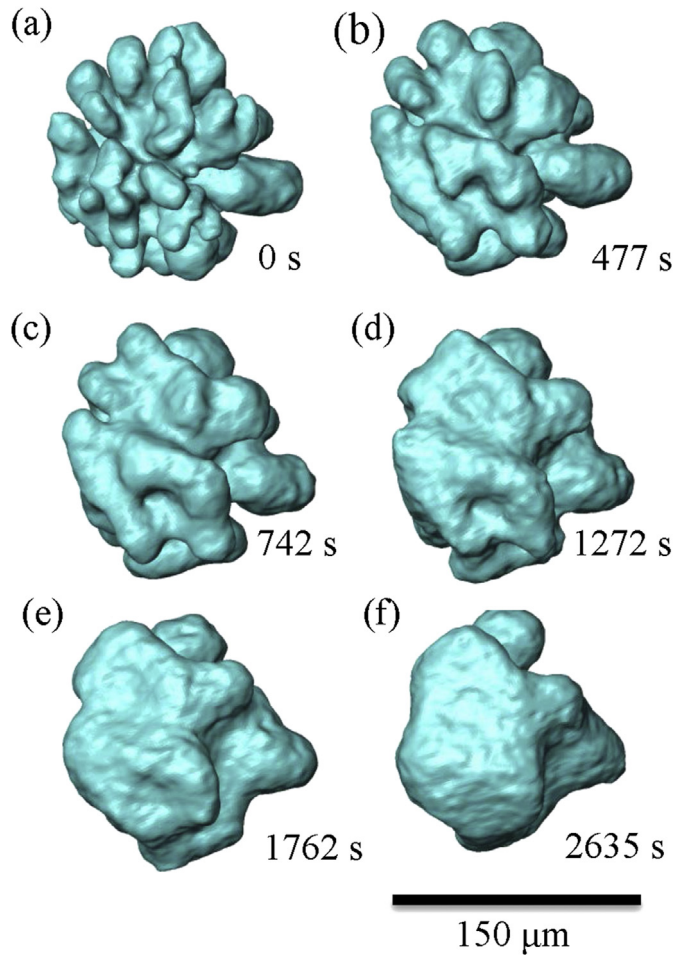


Fig. 4. Dendritic evolution of α -Mg in Mg-38 wt%Zn alloy during isothermal coarsening at 410 °C. Initial solidification cooling rate was 25 °C/min.

many split tips whereas at a cooling rate of 25 °C/min Fig. 4(a), the seaweed structure contains fewer tips. From this observation, it can be inferred that these morphological variations in seaweed structure significantly affect coarsening rates; fewer tips coarsen faster. In other words, seaweed structures do not follow cooling-rate self-similarity if the morphologies are significantly different. It was discussed in Section 3.1.2 that the microstructure at 25 wt%Zn might also not be truly dendritic since each grain contains more than 18 branches. However, the basal plane is clearly six-fold symmetry, which appears to allow for the occurrence of cooling-rate self-similarity. In future research, similar 4D coarsening experiments should be performed on a Mg-20 wt%Zn alloy in order to measure the coarsening rate constant on a grain that has perfect hcp dendritic microstructure [48].

Another factor influencing the coarsening rate constant could be the difference in fraction solid between the two alloys (0.38 vs 0.23 for Mg-25 wt%Zn and Mg-38 wt%Zn). However, since coarsening is driven by diffusion in the liquid and at both solid fractions the grains are mostly separated from each other, the effect of neighbours is minimized. The effect of solid fraction on coarsening in Mg is best investigated using phase-field models since detailed microstructure predictions are readily available. The experimental results found in this study are invaluable for validating such models.

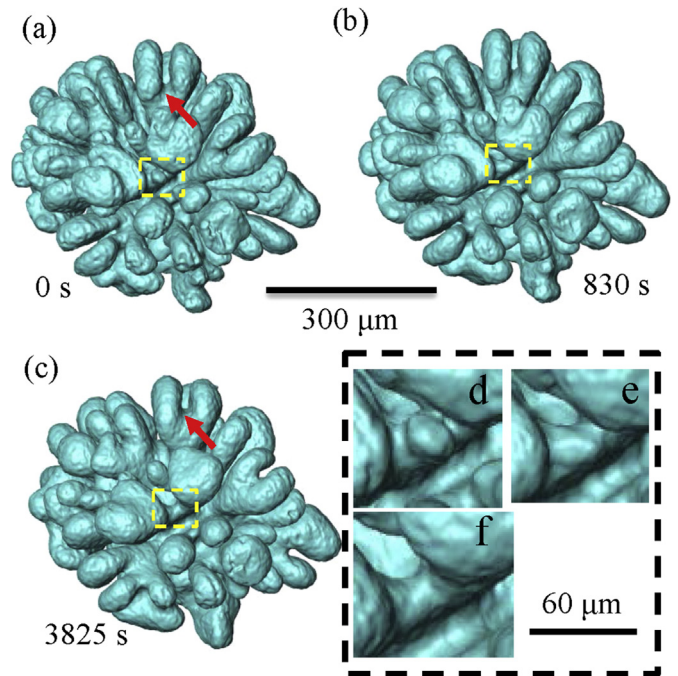


Fig. 5. Dendritic evolution of α -Mg in Mg-38 wt%Zn alloy during isothermal coarsening at 410 °C. Initial solidification cooling rate was 3 °C/min. The enlarged regions, as indicated by rectangle in (a), (b) and (c), are shown in (d), (e), (f), respectively.

3.2.3. Distribution and evolution of curvatures

Local curvature is a frequently-used measure to describe the evolution in the dendrite morphology that is associated with the coarsening process. The two principal curvatures at any point on the surface are defined as $k_1 = 1/R_1$ and $k_2 = 1/R_2$ (with pre-definition of $k_2 \geq k_1$), here R_1 and R_2 are the local principal radii of curvature. These measures can then be translated to mean curvature, H , defined as $H = 0.5 \times (k_1 + k_2)$, and Gauss curvature, K , defined as $K = k_1 \times k_2$. The two principal curvatures can be plotted on a figure contoured by the probability of those curvatures being in the analysed domain, forming the so-called Interfacial Shape Distribution (ISD) [18]. According to the description of ISD, morphologies can be divided into 3 main groups, elliptic shape toward the solid ($k_2 > 0, k_1 > 0$; region 1), hyperbolic shape toward the solid ($k_2 > 0, k_1 < 0$; region 2 and 3), and elliptic shape toward the liquid ($k_2 < 0, k_1 < 0$; region 4) [11,56]. Various interface morphologies can coexist in a single dendrite. For example, the elliptic shape in region 1 is mostly representative of the tips of dendritic branches, the solid hyperbolic interfaces (or saddle shape) in region 2 are usually an indication of the sides of dendritic branches, while the liquid hyperbolic interfaces in region 3 are mostly representative of the roots of dendritic branches.

Fig. 8 shows the evolution of the ISDs for dendrite D4 in Mg-38 wt%Zn during isothermal coarsening. In this figure, the red areas have the highest probability, identifying the most probable interfacial shape. At the start of the isothermal hold, Fig. 8(a), the probability distribution is quite uniform, i.e. no dominant shape exists within the dendrite. As coarsening progresses, the shape of the distribution is seen to move towards the regions with $k_2 = k_1 = 0$, as the larger curvature regions disappear along the dendrite tips. Further, the probability of elliptic interfaces also decreased gradually with time as the probability distribution moves towards the vertical axis ($k_2 = 0$). This is believed to be associated with the filling of the grooves between the dendrite branches, first transitioning to saddle-shape and then evolving to

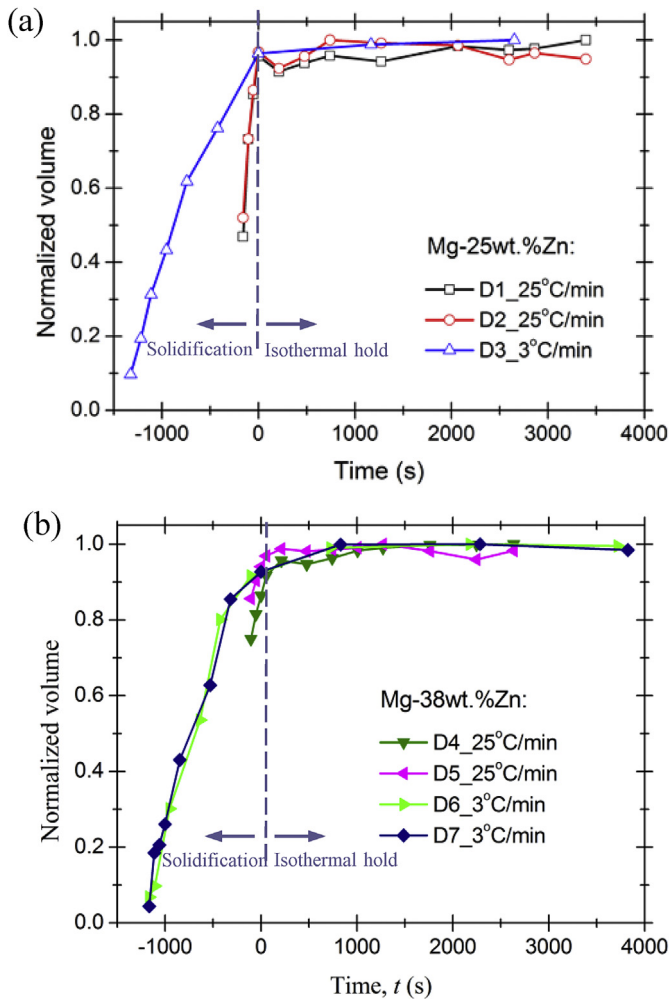


Fig. 6. Normalized volume of individual dendrite in (a) Mg-25 wt%Zn and (b) Mg-38 wt%Zn alloys. The time when the isothermal hold started was set to 0 s for both (a) and (b); negative time in (a) represents the solidification stage.

planar-like as the branches become merged. The evolution of ISDs in Mg dendrites is, in general, similar to that observed in equiaxed dendrites in Al alloys [56]. Note that the tails of the shapes in Fig. 8 can be attributed to noise in the tomographs which creates very fine dimples in the dendrite surface (coloured dots in Fig. 9(a–d)), illustrating that even more advanced, combined filtering and segmentation routines are required. However, since the noise is evenly distributed, it should not change the general trends shown in Figs. 8–9.

The surface of the Mg-38 wt%Zn dendrite (cooled at 25°C/min) with ISDs shown in Fig. 8 is rendered in Fig. 9 using the local values of both the mean curvature, H (images a,b) and Gauss curvature, K (images c,d), before and after isothermal hold. In these images, the red and blue colours correspond to large positive and negative curvatures, respectively. Looking first at the mean curvature, Fig. 9 (a, b), the tips have a strong positive curvature (red, convex), while the negative curvature (blue, concave) is present mostly within the branch roots at the beginning of the isothermal hold. The evolution in the distribution of mean curvature is shown in Fig. 9 (e). The initial mean curvature prior to coarsening (blue curve), shows a normal distribution with an asymmetric peak that is positive. This shape is qualitatively similar to that of Sn dendrites in Pb-Sn alloy measured by Voorhees et al. [17]. As coarsening progresses, the distribution evolves, becoming narrow and with a peak that shifts

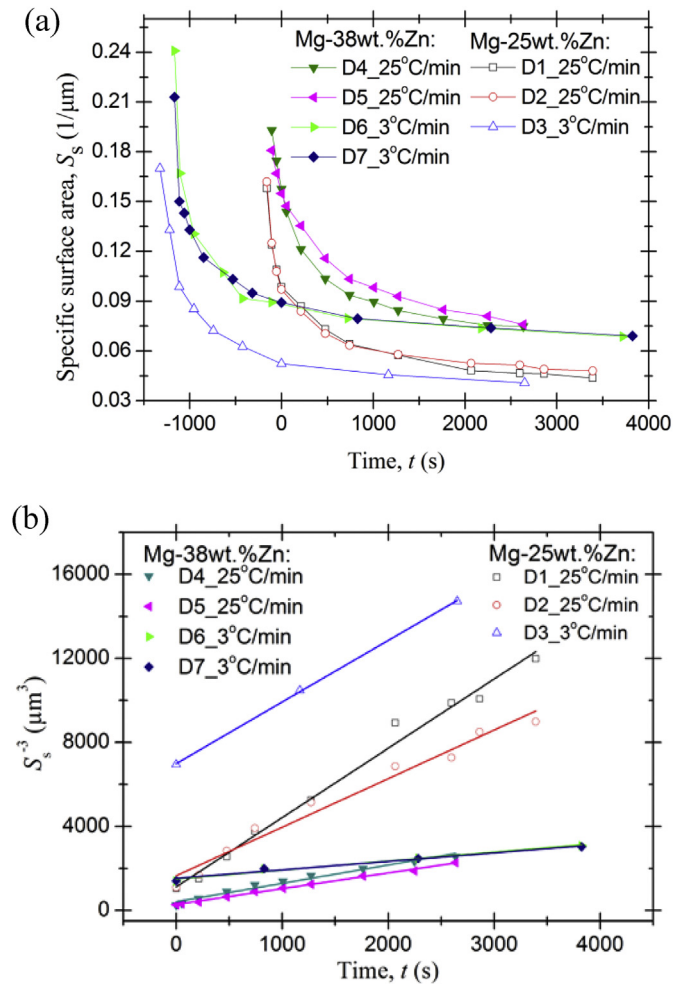


Fig. 7. Evolution of specific surface area (S_s) as a function of time during solidification and isothermal hold: (a) plot of S_s with time t ; (b) plot of S_s^{-3} with time t ; the time when the isothermal hold started was set to 0 s for both (a) and (b); negative time in (a) represents the solidification stage. Solid lines in (b) are the fitting lines for each dendrite.

towards zero. The curvature evolution quantified in Fig. 9(e) is occurring because the dendrite branches are disappearing via coarsening Mechanisms 1 and 2, causing the dendrite's surface to become flatter. The evolution of the curvatures are very similar to those observed in the solidification of Al-Cu where coarsening is accompanied with the dendritic growth [1].

Prior studies have shown that the mean curvature is sometimes insufficient to fully describe the evolution of microstructural morphology with time [17]. For example, the saddle-shaped interfaces with $k_1 < 0$, $k_2 > 0$ at dendrites roots sometimes are associated with a zero mean curvature value, suggesting these saddle-shaped interfaces are not subject to coarsening, which can be misleading. The Gauss curvature provides additional information to resolve such details. As can be seen in Fig. 9 (c,d), the Gauss curvature evolves qualitatively in a similar manner to the mean curvature; the regions with high or low Gauss curvatures at the start of the isothermal hold become reduced. This can also be seen in the quantified distribution of the Gauss curvatures, Fig. 9 (f), where the curves gradually become narrower as the isothermal hold time is increased, together with an increase in the peak value. It is most likely that this occurrence is related to the evolution of saddle-shaped surfaces, with the grooves between the neighbouring branches disappearing due to the remelting of small branches and

Table 1
Coarsening rate values evaluated by Equation (1) for Mg-Zn alloys.

Coarsening rate K_c ($\mu\text{m}^3/\text{s}$)	Mg-25 wt%			Mg-38 wt%Zn			
	25 °C/min		3 °C/min	25 °C/min		3 °C/min	
	D1	D2	D3	D4	D5	D6	D7
	3.29 ± 0.13	2.31 ± 0.14	2.93 ± 0.04	0.87 ± 0.04	0.75 ± 0.01	0.42 ± 0.04	0.41 ± 0.04

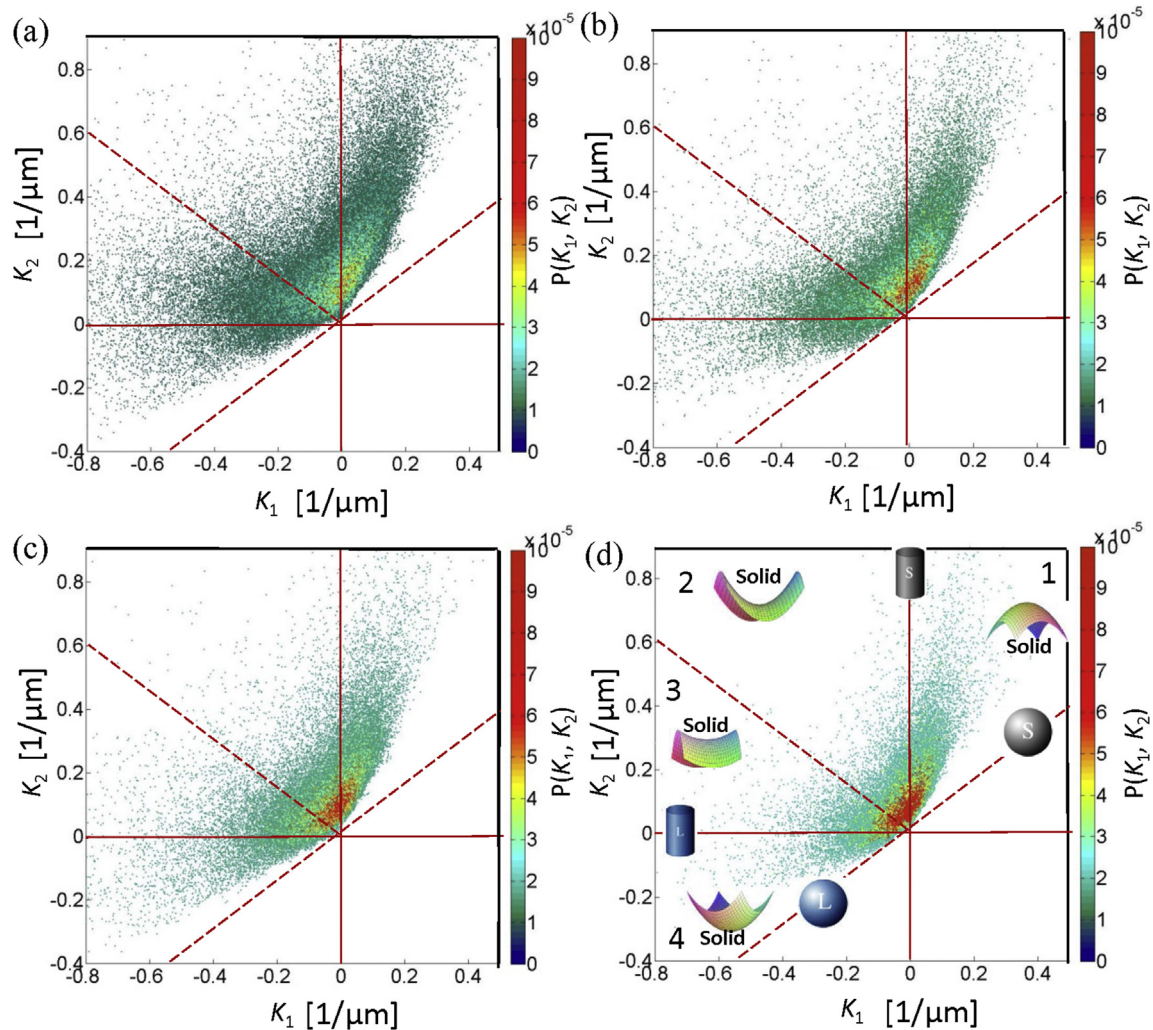


Fig. 8. Distribution of principle curvatures of dendrite in Mg-38 wt%Zn alloy during isothermal coarsening for (a) 0 s, (b) 477 s, (c) 1272 s, and (d) 2635 s. Initial cooling rate was 3 °C/min when the dendrite was formed. The insets indicating the interface shape are cited from Ref. [46].

the coalescence of the adjacent branches. Note that although the analysis of the curvature discussed in Figs. 8 and 9 focused on a dendrite from the Mg-38 wt%Zn alloy cooled at 25 °C/min, the same trends apply for both alloy compositions and cooling rates.

4. Conclusions

In this study, the isothermal coarsening of Mg-Zn hcp was directly observed and quantified using *in situ* fast synchrotron X-ray tomography. The influence of two key parameters, solute composition and initial cooling rate, was investigated. The 3D observations suggested that the coarsening of the hcp dendrites is dominated by the re-melting of small branches, and the coalescence of the neighbouring branches. Zn content was found to have a

large impact on the solidification morphology, changing the six-fold symmetry of the 25 wt%Zn to a highly branched or seaweed structure at 38 wt%Zn.

The evolution of individual dendrites was quantified in terms of specific surface area (S_s), principal curvatures, mean curvature and Gauss curvature to capture the coarsening process. S_s was found to scale inversely with time, with a relationship of $\sim t^{-1/3}$, and was path independent for the Mg-25 wt%Zn samples with dendritic microstructure as the initial cooling rate during solidification did not strongly influence the coarsening rate. However, path independence was not observed for the Mg-38 wt%Zn samples because of the change in solidification morphology to a seaweed microstructure. This led to large differences in S_s and its evolution both between the two alloy compositions and within the Mg-38 wt%Zn

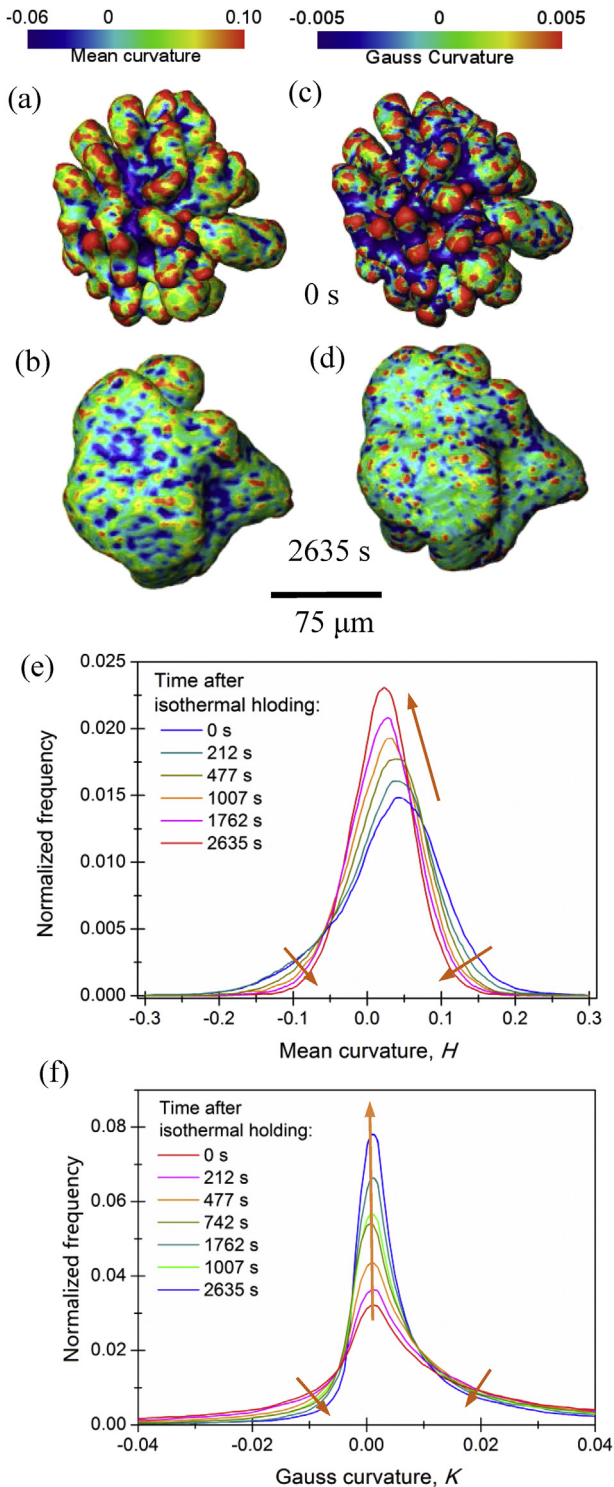


Fig. 9. Distribution of Mean ((a), (b), (e)) and Gauss ((c), (d), (f)) curvature of dendrite as a function of time in Mg-38 wt%Zn. The initial solidification cooling rate was 25 °C/min, under which the dendrite was formed.

for the different cooling rates. As coarsening advanced, the mean curvature was observed to shift gradually from its initial position towards zero, while the frequency of the Gauss curvature with zero value, representing the distribution peak, increased in size. The experimental results acquired in this work can be used to both inform and validate numerical models of Mg alloy semi-solid

dendritic coarsening.

Data statement

A representative sample of research data from the experiments along with the plot data for the graphs in this manuscript is provided in supplementary material available at <http://dx.doi.org/10.1016/j.actamat.2016.10.022>.

Acknowledgements

The authors acknowledge the use of facilities and support provided by the Research Complex at Harwell, and funded in part by the EPSRC (EP/I02249X/1, EP/K007734/1, and EP/M009688/1), and thank the Diamond Light Source for providing the beamtime (MT13302-1) and staff at I13 beamline (Drs. Rau, Wanelik, Cipiccia and Marathe) for technical assistance.

References

- [1] N. Limodin, L. Salvo, E. Boller, M. Suery, M. Felberbaum, S. Gaillieue, K. Madi, In situ and real-time 3-D microtomography investigation of dendritic solidification in an Al-10 wt% Cu alloy, *Acta Mater.* 57 (7) (2009) 2300–2310.
- [2] M. Chen, T.Z. Kattamis, Dendrite coarsening during directional solidification of Al-Cu-Mn alloys, *Mater. Sci. Eng. A* 247 (1–2) (1998) 239–247.
- [3] P.R. Goulart, W.R. Osorio, J.E. Spinelli, A. Garcia, Dendritic microstructure affecting mechanical properties and corrosion resistance of an Al-9wt% Si alloy, *Mater. Manuf. Process.* 22 (3) (2007) 328–332.
- [4] W.R. Osorio, P.R. Goulart, G.A. Santos, C. Moura Neto, A. Garcia, Effect of dendritic arm spacing on mechanical properties and corrosion resistance of Al 9 Wt Pct Si and Zn 27 Wt Pct Al alloys, *Metall. Mater. Trans. A* 37A (8) (2006) 2525–2538.
- [5] P.D. Lee, J.D. Hunt, Hydrogen porosity in directional solidified aluminium-copper alloys: In situ observation, *Acta Mater.* 45 (10) (1997) 4155–4169.
- [6] D.M. Maijer, Y.X. Gao, P.D. Lee, T.C. Lindley, T. Fukui, A through-process model of an A356 brake caliper for fatigue life prediction, *Metall. Mater. Trans. A* 35A (10) (2004) 3275–3288.
- [7] D.H. Kirkwood, Semisolid metal processing, *Int. Mater. Rev.* 39 (5) (1994) 173–189.
- [8] K.M. Kareh, P.D. Lee, R.C. Atwood, T. Connolly, C.M. Gourlay, Revealing the micromechanisms behind semi-solid metal deformation with time-resolved X-ray tomography, *Nat. Commun.* 5 (2014).
- [9] S. Karagadde, P.D. Lee, B. Cai, J.L. Fife, M.A. Azeem, K.M. Kareh, C. Puncreobutr, D. Tsivoulas, T. Connolly, R.C. Atwood, Transgranular liquation cracking of grains in the semi-solid state, *Nat. Commun.* 6 (2015).
- [10] S.P. Marsh, M.E. Glicksman, Overview of geometric effects on coarsening of mushy zones, *Metall. Mater. Trans. A* 27 (3) (1996) 557–567.
- [11] D. Kammer, P.W. Voorhees, The morphological evolution of dendritic microstructures during coarsening, *Acta Mater.* 54 (6) (2006) 1549–1558.
- [12] P.W. Voorhees, M.E. Glicksman, Ostwald ripening during liquid-phase Sintering- Effect of volume fraction on coarsening kinetics, *Metall. Trans. A* 15 (6) (1984) 1081–1088.
- [13] P.W. Voorhees, Ostwald Ripening of two-phase mixtures, *Annu. Rev. Mater. Res.* 22 (1992) 197–215.
- [14] D.H. Kirkwood, A simple model for dendrite arm coarsening during solidification, *Mater. Sci. Eng. A* 73 (1–2) (1985) L1–L4.
- [15] K.P. Young, D.H. Kirkwood, Dendrite arm spacings of aluminum-copper alloys solidified under steady state conditions, *Metall. Trans.* 6 (1) (1975) 197–205.
- [16] T.Z. Kattamis, M.C. Flemings, Dendrite structure and grain size of undercooled melts, *Trans. Metall. Soc. AIME* 236 (11) (1966) 1523.
- [17] J. Alkemper, P.W. Voorhees, Three-dimensional characterization of dendritic microstructures, *Acta Mater.* 49 (5) (2001) 897–902.
- [18] R. Mendoza, J. Alkemper, P.W. Voorhees, The morphological evolution of dendritic microstructures during coarsening, *Metall. Mater. Trans. A* 34 (3) (2003) 481–489.
- [19] L. Ratke, C. Beckermann, Concurrent growth and coarsening of spheres, *Acta Mater.* 49 (19) (2001) 4041–4054.
- [20] F.D. Fischer, J. Svoboda, E. Gamsjaeger, E.R. Oberaigner, From distribution functions to evolution equations for grain growth and coarsening, *Acta Mater.* 56 (19) (2008) 5395–5400.
- [21] L. Ratke, A. Genau, Evolution of specific surface area with solid fraction during solidification, *Acta Mater.* 58 (12) (2010) 4207–4211.
- [22] T. Philippe, P.W. Voorhees, Ostwald ripening in multicomponent alloys, *Acta Mater.* 61 (11) (2013) 4237–4244.
- [23] J. Wang, G. Yang, Phase-field modeling of isothermal dendritic coarsening in ternary alloys, *Acta Mater.* 56 (17) (2008) 4585–4592.
- [24] L.K. Agesen, J.L. Fife, E.M. Lauridsen, P.W. Voorhees, The evolution of interfacial morphology during coarsening: a comparison between 4D experiments and phase-field simulations, *Scr. Mater.* 64 (5) (2011) 394–397.

- [25] D. Kammer, R. Mendoza, P.W. Voorhees, Cylindrical domain formation in topologically complex structures, *Scr. Mater.* 55 (1) (2006) 17–22.
- [26] J.L. Fife, P.W. Voorhees, Self-similar microstructural evolution of dendritic solid-liquid mixtures during coarsening, *Scr. Mater.* 60 (10) (2009) 839–842.
- [27] A.L. Genau, P.W. Voorhees, The morphological evolution of low volume fraction tin dendrites during coarsening, *Metall. Mater. Trans. A* 44A (1) (2013) 406–418.
- [28] W. Bender, L. Ratke, Ostwald ripening of liquid phase sintered Cu-Co dispersions at high volume fractions, *Acta Mater.* 46 (4) (1998) 1125–1133.
- [29] I. Seyhan, L. Ratke, W. Bender, P.W. Voorhees, Ostwald ripening of solid-liquid Pb-Sn dispersions, *Metall. Mater. Trans. A* 27 (9) (1996) 2470–2478.
- [30] D.J. Rowenhorst, J.P. Kuang, K. Thornton, P.W. Voorhees, Three-dimensional analysis of particle coarsening in high volume fraction solid-liquid mixtures, *Acta Mater.* 54 (8) (2006) 2027–2039.
- [31] O. Pompe, M. Rettenmayr, Microstructural changes during quenching, *J. Cryst. Growth* 192 (1–2) (1998) 300–306.
- [32] S. Terzi, L. Salvo, M. Suery, A. Dahle, E. Boller, In situ microtomography investigation of microstructural evolution in Al-Cu alloys during holding in semi-solid state, *Trans. Nonferrous Metals Soc. China* 20 (2010) S734–S738.
- [33] E.D. Manson-Whitton, I.C. Stone, J.R. Jones, P.S. Grant, B. Cantor, Isothermal grain coarsening of spray formed alloys in the semi-solid state, *Acta Mater.* 50 (10) (2002) 2517–2535.
- [34] J.W.K. van Boggelen, D.G. Eskin, L. Katgerman, First stages of grain coarsening in semi-solid Al-Cu alloys, *Scr. Mater.* 49 (7) (2003) 717–722.
- [35] R. Mendoza, I. Savin, K. Thornton, P.W. Voorhees, Topological complexity and the dynamics of coarsening, *Nat. Mater.* 3 (6) (2004) 385–388.
- [36] W. Wang, P.D. Lee, M. McLean, A model of solidification microstructures in nickel-based superalloys: predicting primary dendrite spacing selection, *Acta Mater.* 51 (10) (2003) 2971–2987.
- [37] S.G.R. Brown, Simulation of diffusional composite growth using the cellular automaton finite difference (CAFD) method, *J. Mater. Sci.* 33 (19) (1998) 4769–4773.
- [38] W.J. Boettinger, J.A. Warren, C. Beckermann, A. Karma, Phase-field simulation of solidification, *Annu. Rev. Mater. Res.* 32 (2002) 163–194.
- [39] I. Steinbach, Phase-field models in materials science, *Model. Simul. Mater. Sci. Eng.* 17 (7) (2009).
- [40] C. Beckermann, H.J. Diepers, I. Steinbach, A. Karma, X. Tong, Modeling melt convection in phase-field simulations of solidification, *J. Comput. Phys.* 154 (2) (1999) 468–496.
- [41] B. Bottger, J. Eiken, M. Ohno, G. Klaus, M. Fehlbier, R. Schmid-Fetzer, I. Steinbach, A. Buehrig-Polaczek, Controlling microstructure in magnesium alloys: a combined thermodynamic, experimental and simulation approach, *Adv. Eng. Mater.* 8 (4) (2006) 241–247.
- [42] B. Cai, S. Karagadde, L. Yuan, T.J. Marrow, T. Connolly, P.D. Lee, In situ synchrotron tomographic quantification of granular and intragranular deformation during semi-solid compression of an equiaxed dendritic Al-Cu alloy, *Acta Mater.* 76 (2014) 371–380.
- [43] B. Cai, P.D. Lee, S. Karagadde, T.J. Marrow, T. Connolly, Time-resolved synchrotron tomographic quantification of deformation during indentation of an equiaxed semi-solid granular alloy, *Acta Mater.* 105 (2016) 338–346.
- [44] A.B. Phillion, R.W. Hamilton, D. Fuloria, A.C.L. Leung, P. Rockett, T. Connolly, P.D. Lee, In situ X-ray observation of semi-solid deformation and failure in Al-Cu alloys, *Acta Mater.* 59 (4) (2011) 1436–1444.
- [45] N. Limodin, L. Salvo, M. Suery, M. DiMichiel, In situ investigation by X-ray tomography of the overall and local microstructural changes occurring during partial remelting of an Al-15.8 wt% Cu alloy, *Acta Mater.* 55 (9) (2007) 3177–3191.
- [46] J.L. Fife, J.W. Gibbs, E.B. Gulsoy, C.L. Park, K. Thornton, P.W. Voorhees, The dynamics of interfaces during coarsening in solid-liquid systems, *Acta Mater.* 70 (2014) 66–78.
- [47] S.S. Shuai, E.Y. Guo, A. Phillion, M.D. Callaghan, T. Jing, P.D. Lee, Fast synchrotron X-ray tomography quantification of the dendritic evolution during the solidification of Mg-Sn alloys, *Acta Mater.* 118 (2016) 260–269.
- [48] M. Yang, S.M. Xiong, Z. Guo, Effect of different solute additions on dendrite morphology and orientation selection in cast binary magnesium alloys, *Acta Mater.* 112 (2016) 261–272.
- [49] M. Wang, Y. Xu, Q. Zheng, S. Wu, T. Jing, N. Chawla, Dendritic growth in Mg-Based alloys: phase-field simulations and experimental verification by X-ray synchrotron tomography, *Metall. Mater. Trans. A* 45A (5) (2014) 2562–2574.
- [50] T. Haxhimali, A. Karma, F. Gonzales, M. Rappaz, Orientation selection in dendritic evolution, *Nat. Mater.* 5 (8) (2006) 660–664.
- [51] S. Shuai, E. Guo, Q. Zheng, M. Wang, T. Jing, Y. Fu, Three-dimensional α -Mg dendritic morphology and branching structure transition in Mg-Zn alloys, *Mater. Charact.* 118 (2016) 304–308.
- [52] S.S. Shuai, E.Y. Guo, M.Y. Wang, M.D. Callaghan, T. Jing, Q.W. Zheng, P.D. Lee, Anomalous α -Mg dendrite growth during directional solidification of a Mg-Zn alloy, *Metall. Mater. Trans. A* 47A (9) (2016) 4368–4373.
- [53] B. Li, H.D. Brody, A. Kazimirov, Real time synchrotron microradiography of dendrite coarsening in Sn-13 wt pct Bi alloy, *Metall. Mater. Trans. A* 38A (3) (2007) 599–605.
- [54] S. Terzi, L. Salvo, M. Suery, A.K. Dahle, E. Boller, Coarsening mechanisms in a dendritic Al-10% Cu alloy, *Acta Mater.* 58 (1) (2010) 20–30.
- [55] R. Mendoza, Morphological and Topological Characterization of Coarsened Dendritic Microstructures, PHD Thesis, Northwestern University, 2004.
- [56] J.L. Fife, P.W. Voorhees, The morphological evolution of equiaxed dendritic microstructures during coarsening, *Acta Mater.* 57 (8) (2009) 2418–2428.
- [57] A. Einstein, The motion of elements suspended in static liquids as claimed in the molecular kinetic theory of heat, *Ann. Phys.* 17 (8) (1905) 549–560.
- [58] I.M. Lifshitz, V.V. Slyozov, The kinetics of precipitation from supersaturated solid solutions, *J. Phys. Chem. Solids* 19 (1–2) (1961) 35–50.
- [59] C. Wagner, Theorie der alterung von niederschlagen durch umlosen (Ostwald-reifung), *Z. Fur Elektrochem.* 65 (7–8) (1961) 581–591.
- [60] J.D. Thompson, E.B. Gulsoy, P.W. Voorhees, Self-similar coarsening: a test of theory, *Acta Mater.* 100 (2015) 282–289.